

LETTER • **OPEN ACCESS**

## Sentinel-1 observation frequency significantly increases burnt area detectability in tropical SE Asia

To cite this article: Joao M B Carreiras *et al* 2020 *Environ. Res. Lett.* **15** 054008

View the [article online](#) for updates and enhancements.



## LETTER

## OPEN ACCESS

RECEIVED  
22 August 2019

REVISED  
14 February 2020

ACCEPTED FOR PUBLICATION  
18 February 2020

PUBLISHED  
29 April 2020

Original content from this work may be used under the terms of the [Creative Commons Attribution 4.0 licence](#).

Any further distribution of this work must maintain attribution to the author(s) and the title of the work, journal citation and DOI.



# Sentinel-1 observation frequency significantly increases burnt area detectability in tropical SE Asia

Joao M B Carreiras<sup>1</sup> , Shaun Quegan<sup>1</sup> , Kevin Tansey<sup>2</sup> and Susan Page<sup>2</sup>

<sup>1</sup> National Centre for Earth Observation, University of Sheffield, Sheffield, United Kingdom

<sup>2</sup> Centre for Landscape and Climate Research, School of Geography, Geology & the Environment, University of Leicester, Leicester, United Kingdom

E-mail: [j.carreiras@sheffield.ac.uk](mailto:j.carreiras@sheffield.ac.uk)

**Keywords:** burnt area, tropics, Sentinel-1, radar, machine learning, Indonesia

Supplementary material for this article is available [online](#)

## Abstract

Frequent cloud cover in the tropics significantly affects the observation of the surface by satellites. This has enormous implications for current approaches that estimate greenhouse gas (GHG) emissions from fires or map fire scars. These mainly employ data acquired in the visible to middle infrared bands to map fire scars or thermal data to estimate fire radiative power and consequently derive emissions. The analysis here instead explores the use of microwave data from the operational Sentinel-1A (S-1A) in dual-polarisation mode (VV and VH) acquired over Central Kalimantan during the 2015 fire season. Burnt areas were mapped in three consecutive periods between August and October 2015 using the random forests machine learning algorithm. In each mapping period, the omission and commission errors of the unburnt class were always below 3%, while the omission and commission errors of the burnt class were below 20% and 5% respectively. Summing the detections from the three periods gave a total burnt area of ~1.6 million ha, but this dropped to ~1.2 million ha if using only a pair of pre- and post-fire season S-1A images. Hence the ability of Sentinel-1 to make frequent observations significantly increases fire scar detection. Comparison with burnt area estimates from the Moderate Resolution Imaging Spectroradiometer (MODIS) burnt area product at 5 km scale showed poor agreement, with consistently much lower estimates produced by the MODIS data—on average 14%–51% of those obtained in this study. The method presented in this study offers a way to reduce the substantial errors likely to occur in optical-based estimates of GHG emissions from fires in tropical areas affected by substantial cloud cover.

## 1. Introduction

Data acquired by orbital platforms are the only way of routinely, consistently and affordably observing and monitoring land processes at large spatial and long temporal scales (Harris *et al* 2012, Hansen *et al* 2013, Tyukavina *et al* 2015, Reiche *et al* 2016). As a result, estimates of carbon released by fires rely on burnt area mapping (Giglio *et al* 2013), identification of hotspots (Randerson *et al* 2012) or estimates of fire radiative power output (Wooster *et al* 2012) from satellite data. Currently, the vast majority of methods to map burnt areas rely on automatic or semi-automatic processing of optical data from high or moderate spatial and

temporal resolution satellite data (Gregoire *et al* 2003, Simon *et al* 2004, Silva *et al* 2005, Miettinen *et al* 2007, Giglio *et al* 2009, 2013, Sedano *et al* 2013). Furthermore, ongoing projects are providing global and repetitive burnt area mapping and derived emissions, e.g. the Global Fire Emissions Database (GFED4; <http://globalfiredata.org>) (van der Werf *et al* 2010, Randerson *et al* 2012, Giglio *et al* 2013) and the European Space Agency's (ESA) Climate Change Initiative-Fire (CCI-Fire; <http://esa-fire-cci.org/>) (Chuvieco *et al* 2016). Most of the fire activity is observed across the tropics, either as a consequence of local livelihoods (shifting agriculture in Africa) or land clearing for agriculture (South America and Southeast

Asia) (Lambin *et al* 2003). In these regions, frequent cloud cover and haze and smoke from the fire activity itself can hamper observation of the surface by optical sensors and limit their ability to map fire scars (Schroeder *et al* 2008).

Synthetic Aperture Radar (SAR) is well placed to provide this information due to its insensitivity to cloud and haze. Current spaceborne SAR sensors acquire day-and-night data using microwave radiation at various frequencies and incidence angles (Moreira *et al* 2013). The measured backscatter intensity depends on characteristics of the sensor, such as frequency and incidence angle, but also on the size, structure and dielectric properties of the scatterers (Woodhouse 2006). Three main scattering mechanisms can be associated with the interaction of microwave radiation and distributed targets over a ground surface: surface, volume and double bounce scattering (Richards 2009), whose relative importance depends on land cover and its structure and status, together with the observing frequency and polarisation.

For the C-band data used in this paper, the dominant effects for undisturbed dense tropical forest are scattering and attenuation by leaves and twigs in the canopy, with little return from the surface or double-bounce. The random orientation of the scatterers leads to significant depolarisation and hence VH backscatter. In contrast, if fire removes these small scatterers and allows penetration to ground level, the nature of the return will change from volume scattering to a complicated mixture of surface and double bounce scattering, perhaps with some volume scattering. The make-up of the backscatter will then depend on surface roughness, surface slope, soil moisture, surface detritus and any remnant vegetation. A significant drop in VH backscatter would be expected, while the behaviour of VV backscatter is hard to predict as it depends on many unknown factors.

A small number of studies have shown the potential of SAR data to map forest fires in tropical regions. Siegert and Hoffmann (2000) used mainly multi-temporal data acquired by the single-polarisation (VV) C-band SAR onboard ESA's European Remote Sensing (ERS-2) satellite to map the extensive forest fires in East Kalimantan in 1998; multi-temporal SAR data (before and after the fire) were subjected to principal component analysis and visually interpreted to map burnt areas, but no information is provided about the accuracy of the method. Menges *et al* (2004) studied the ability of SAR data to discriminate savanna fires in Australia (100 km east of Darwin) using data collected in 2000 from the National Aeronautics and Space Administration (NASA) Jet Propulsion Laboratory (JPL) AIRSAR multi-frequency (C-, L- and P-band) instrument. The C-band data provided some degree of separability between burnt and unburnt areas, whereas L- and P-band were ineffective because the low-intensity fires characteristic of the region did not produce enough damage to be

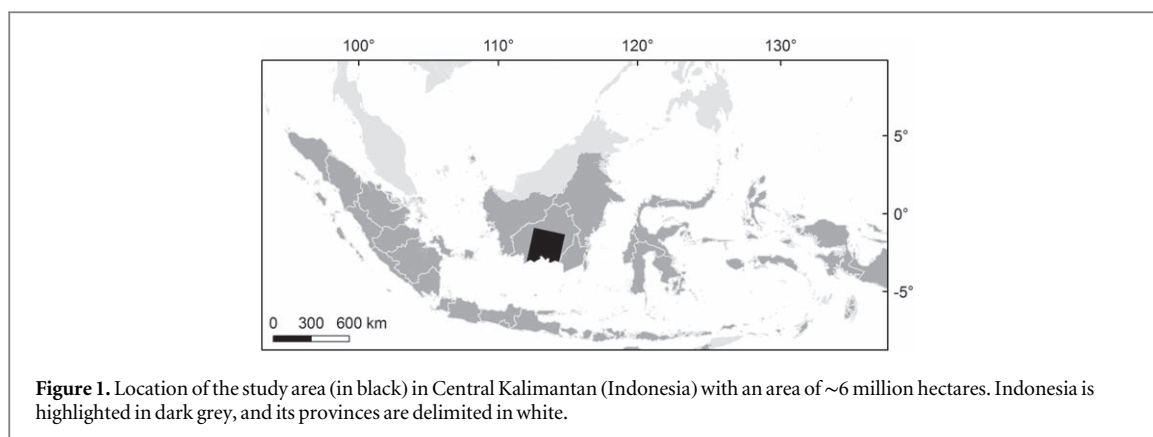
detected at lower frequencies. Lohberger *et al* (2018) used Sentinel-1 imagery acquired over large areas of Indonesia (Sumatra, Kalimantan and West Papua) to map the total burnt area during the 2015 fire season, with the authors reporting an overall accuracy of 84% but without any information about class-specific errors.

The Sentinel-1A C-band SAR was the first of a series of operational Earth Observation satellites to be launched in order to provide the European Union with monitoring capabilities for environment and security (Butler 2014). Sentinel-1A and 1B were launched in April 2014 and April 2016, respectively, and are in the same orbit but 180° apart. At full operational capacity, the system provides global coverage every 12 days by each satellite in dual-polarization (VV + VH) Interferometric Wide-Swath (IW) mode at 20 m (range) × 22 m (azimuth) ground resolution (Torres *et al* 2012). This is the first time that continual access to high-resolution all-weather remote sensing data over tropical regions will be provided openly and free of charge. It potentially marks a major change in the role of active microwave sensors in mapping fire scars, which up to now has been very limited and confined to estimating the overall burnt area at the end of the fire season.

The objective of this paper is to explore this potential, by assessing the ability of Sentinel-1A data to map burnt areas in Central Kalimantan during the 2015 fire season, when only Sentinel-1A was in orbit. We compare the overall burnt area obtained when (i) adding detections obtained from Sentinel-1A acquisitions in three sub-periods of the 2015 fire season (13 August–6 September, 6–30 September, 30 September–24 October), and (ii) using only a pair of pre-fire (13 August) and post-fire (24 October) season Sentinel-1A acquisitions.

## 2. Study area

The study area (figure 1) is a Sentinel-1A swath ~250 km wide by ~230 km long (two slices), over Central Kalimantan (Indonesia). This area has been included in several studies estimating the carbon emissions from forest fires during the El Niño events of 1997–98 (Siegert and Hoffmann 2000, Page *et al* 2002) and 2015–16 (Huijnen *et al* 2016, Lohberger *et al* 2018). Around 38% of the study area was initially covered with peat swamp forest, of which a significant proportion had been converted to other land cover/use types by 2015 (Miettinen *et al* 2016). Degraded peat swamp forest occupied 35% of the peatland area, and 21% was covered by tall shrub/secondary forest; only 12% remained as pristine peat swamp forest. Other significant cover types include small-holder areas (10%) and industrial plantations (8%).



### 3. Data

#### 3.1. Sentinel-1A

Sentinel-1A (S-1A) interferometric wide swath (IW) dual-polarisation (VV + VH) single-look complex data over the region are available since May 2015. S-1A IW data are acquired with a 250 km swath, using three sub-swaths with the Terrain Observation with Progressive Scans SAR (TOPSAR) technique (De Zan and Guarnieri 2006) with an incidence angle range of 29° to 46°. Data were downloaded free of charge on eight dates between 9 May and 24 October 2015 spaced every 24 d, to entirely cover the 2015 fire season; acquisition dates are given in table S1 (supplementary information is available online at [stacks.iop.org/ERL/15/054008/mmedia](https://stacks.iop.org/ERL/15/054008/mmedia)). Systematic S-1A IW acquisitions every 12 days were only made from January 2017.

Further processing is required to obtain terrain-corrected and normalised backscatter intensity data with reduced speckle. The single-look complex data was first multi-looked (8 looks in range and two looks in azimuth) to obtain approximately 30 m ground resolution intensity images. We then co-registered the temporal stack to minimise positional mismatch and to allow multi-temporal filtering. Geocoded terrain-corrected images were produced using a rigorous range-Doppler approach, assisted by a 3 arcsec (~90 m) digital elevation model (DEM) obtained from the Shuttle Radar Topography Mission (SRTM) and downloaded from the United States Geological Survey (USGS). Absolute radiometric calibration and radiometric normalisation to sigma nought ( $\sigma^0$ ) were carried out to generate intensity images. Multi-channel filtering (Quegan and Yu 2001) was then applied to the multi-temporal stack of dual-pol intensity images to generate a reduced-speckle dataset without significant loss of spatial resolution. The final processed dataset consists of a time-series of S-1A dual-pol images with 30 m ground resolution speckle-reduced to an equivalent number of looks (ENL) of ~100.

Only four of the eight S-1A IW acquisition dates between May and October 2015 were used to map burnt areas. The S-1A IW acquisitions on 13 August, 6

September, 30 September and 24 October covered a period when over 90% of the active fires were recorded in the region (figure S1 supplementary information). The remaining acquisitions were only used to improve the process of multi-temporal filtering. Seven variables obtained from the S-1A IW data were used as predictors to detect burnt areas: pre-fire and post-fire VV and VH backscatter intensity, difference between post-fire and pre-fire backscatter intensity in VV and VH, and local incidence angle.

#### 3.2. Landsat 8

Landsat 8 Operational Land Imager (OLI) data covering the study area were downloaded free of charge from the USGS. Four scenes are required to cover the area depicted in figure 1: paths 118 and 119, rows 61 and 62. A total of 28 scenes (Collection 1 Level-1) were downloaded, acquired between March and October 2015. Acquisition dates are given in table S2 (supplementary information), along with an estimate of cloud cover. The mean cloud cover over this period is ~60%, so these images are often affected by clouds, cloud shadows and sometimes dense haze. This dataset was used to assist with the selection of training areas known to be affected by fire or unburnt.

#### 3.3. Burnt area maps

Published and freely available burnt area maps covering the same region and period were used to compare with the results from this study. The burnt area map produced by Lohberger *et al* (2018) used Sentinel-1A IW imagery acquired over Indonesia in 2015 and was generated within the scope of ESA Climate Change Initiative-Fire (CCI-Fire) at a resolution of 10 m. The Moderate Resolution Imaging Spectrometer (MODIS) monthly Burned Area product (MCD64A1, collection 6) (Giglio *et al* 2015, 2018) is generated at ~500 m spatial resolution and provides information about the date of burn in each month. This dataset was used to produce maps of burnt area temporally coincident with the periods between S-1A IW acquisitions over the study area.

**Table 1.** The number of burnt and unburnt observations in each pre-fire/post-fire pair of Sentinel-1A Interferometric Wide (IW) swath acquisitions.

Sentinel-1A IW swath acquisitions		Number of observations	
Pre-fire	Post-fire	Burnt	Unburnt
13 August	6 September	190	686
6 September	30 September	250	903
30 September	24 October	100	361
Total		540	1950

## 4. Methods

### 4.1. Training data

An evenly spaced grid of 25 km was overlaid on the Landsat 8 OLI data covering the study area to guide a systematic collection of homogeneous training areas of unburnt or burnt observations. Each observation consisted of a 90 m  $\times$  90 m rectangle. Landsat 8 OLI data were used to select a total of 1,950 observations over invariant unburnt areas between 13 August and 24 October 2015 (Fortier *et al* 2011). Observations of burnt areas were selected between two consecutive dates (hereafter denoted as pre-fire and post-fire dates). These were marked as burnt if a transition from unburnt to burnt was observed between the two dates. The number of observations per consecutive date is given in table 1. A stratified random sampling approach was used to select a subset of 70% of the data for training, with the remainder used for testing.

### 4.2. Mapping burnt areas with random forests

The Random Forests (RF) algorithm (Breiman 2001) was used to discriminate between unburnt and burnt areas, using Sentinel-1A VV and VH intensity as covariates. A RF model is generated as a committee of binary decision trees. Each RF tree is fitted to a bootstrap sample of the original training dataset with replacement. Essentially, only two parameters need to be defined: the number of trees in each RF model and the number of randomly selected covariates to be used at each decision node. Those observations not selected for fitting each RF tree make up the out-of-bag sample and are used to assess the model error. A useful metric obtained when fitting RF models is a variable importance score, which provides a relative measure of which predictors contribute the most to classification accuracy. The randomForest (v4.6-12) R package was used for model fitting and prediction and the randomForestExplainer (v0.10.0) R package was used to obtain information about variable importance in the fitted RF model. A single RF algorithm was fitted to map burnt areas occurring between consecutive dates.

The output from RF gives the proportion of all trees classifying an observation as burnt and unburnt. A threshold value must be assigned to the proportion

voted as burnt in order to classify a pixel as burnt or unburnt. Various criteria can be used to select the best threshold, e.g. the value maximising overall accuracy or Cohen's kappa (Freeman and Moisen 2008) but this always involves a trade-off between omission and commission errors. The selection of the threshold is a decision about an acceptable level of each type of error, and here we chose to limit the commission error to a specific value, in order not to have too high a proportion of false detections.

The RF algorithm was then used to extrapolate to the entire study area. All predictor variables were spatially averaged to the same resolution used to generate the training dataset (0.81 ha = 90 m  $\times$  90 m training areas).

Discrimination performance was estimated using the test subset to generate the confusion matrix corresponding to each period. However, as often happens, the number of samples collected in burnt and unburnt areas is not proportional to the total area of each class (unknown at the beginning of the study). Therefore, the traditional confusion matrix relying on sample counts was corrected using the mapped area of each class, according to Olofsson *et al* (2014).

### 4.3. Comparison with maps of burnt area

Comparison with other burnt area products was made using a systematic grid of 5 km. Only the 5 km cells entirely contained in the study area were used in the analysis ( $n = 2226$ ). The monthly MODIS-based burnt area product (MCD46A1) was aggregated to obtain the burnt area proportion at 5 km scale during each of the S-1A IW periods (table 1). The burnt area maps from S-1A IW were also aggregated to generate estimates of burnt area proportion at 5 km scale. Additionally, the burnt area map from Lohberger *et al* (2018) covering the entire 2015 fire season at a spatial resolution of 10 m was used to compare with the burnt area map generated in this study at 90 m spatial resolution.

## 5. Results

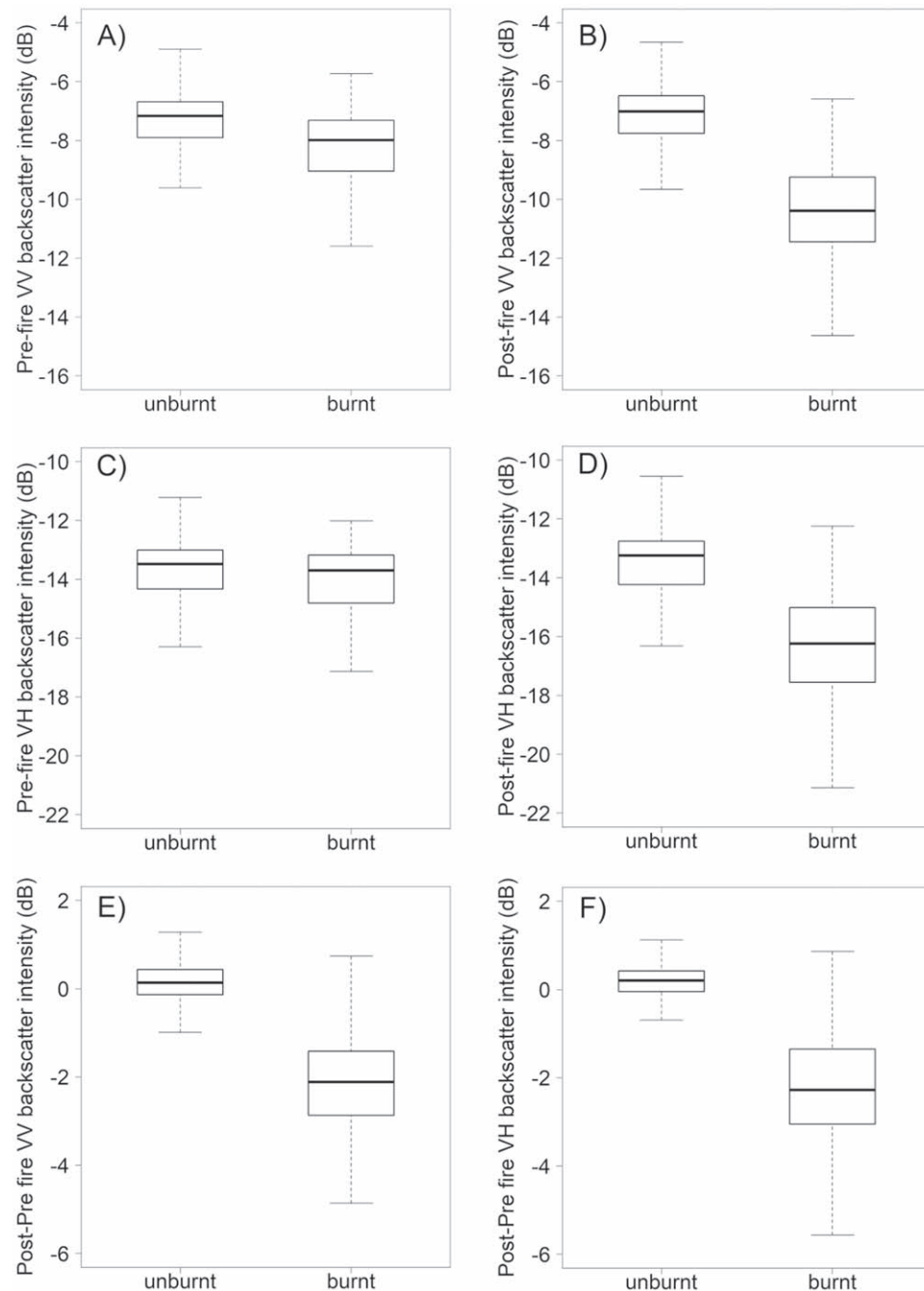
### 5.1. Discrimination of unburnt and burnt areas

Figure 2 depicts the distribution of the values of six variables obtained from the Sentinel-1A IW data. The distributions of the differences in VV and VH  $\sigma^0$  (in dB) between pre-fire and post-fire in unburnt areas have a median value close to zero (figures 2(E) and (F)). In contrast, over burnt areas the median values of VV and VH  $\sigma^0$  before burn are  $-8.0$  dB (figure 2(A)) and  $-13.7$  dB (figure 2(C)), respectively, decreasing to  $-10.4$  dB in VV (figure 2(B)) and  $-16.2$  in VH (figure 2(D)) after burn.

### 5.2. Mapping burnt areas with S-1A IW data

The threshold used to convert from proportion voted as burnt to 2-class maps of burnt and unburnt was





**Figure 2.** Distribution of the values of variables (in dB) obtained from Sentinel-1A Interferometric Wide (IW) swath data over unburnt and burnt locations in the training subset ( $n = 1,742$ ). (A) pre-fire Sentinel-1A IW VV  $\sigma^0$ ; (B) post-fire Sentinel-1A IW VV  $\sigma^0$ ; (C) pre-fire Sentinel-1A IW VH  $\sigma^0$ ; (D) post-fire Sentinel-1A IW VH  $\sigma^0$ ; (E) difference between post-fire and pre-fire  $\sigma^0$  in Sentinel-1A IW VV, (F) difference between post-fire and pre-fire  $\sigma^0$  in Sentinel-1A IW VH. Each boxplot represents the minimum, first quartile, median, third quartile and maximum. The same information using the test subset is shown in figure S2 (supplementary information).

selected by assessing how it affected omission and commission errors and Cohen's kappa (figure 3). Note that the omission error monotonically increases from 0% if the threshold is set to 0 (all trees vote for a pixel to be burnt) to 100% if the threshold is set to 1 (all trees vote for a pixel to be unburnt). The plot also shows a rapid initial decrease in commission error and a concomitant slow increase in omission error. Cohen's kappa exceeds 90% for a wide range of threshold values, thus providing little information to help select

the threshold. We selected the threshold corresponding to a commission error of the burnt class equal to 5.0% (figure 3, horizontal line, threshold = 0.311), which resulted in an omission error of 5.3% (or a detection rate of 94.7%). The relative variable importance score obtained from the fitted RF model showed that the VH and VV backscatter change from pre-fire to post-fire conditions were the most important variables to discriminate burnt from unburnt areas (supplementary information figure S3).

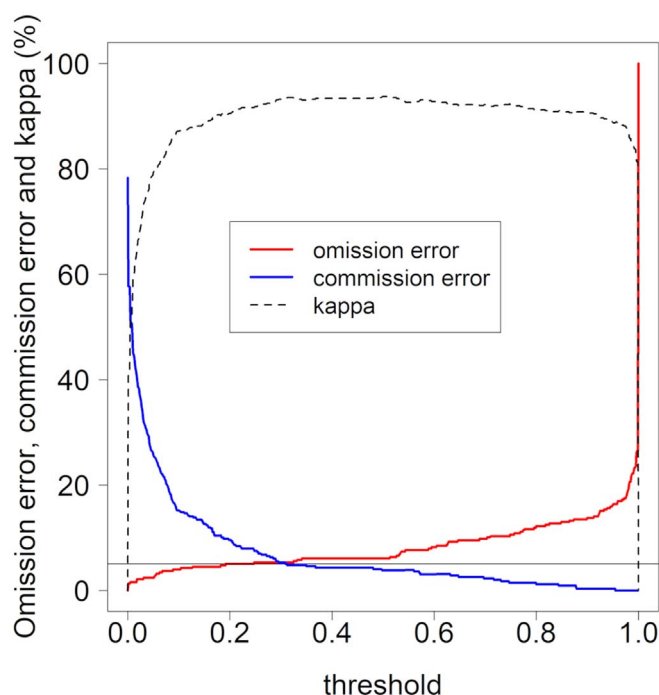


**Figure 3.** The relationship between the threshold and omission and commission errors for the burnt class and Cohen's kappa (a measure of overall accuracy). The horizontal line represents the value of commission error used to set the threshold that discriminates burnt from unburnt observations. Threshold values range from 0 to 1 with increments of 0.001. These relationships were generated with the out-of-bag subset from fitting the random forests model.

**Table 2.** Omission error, commission error, Cohen's kappa and estimated burnt area by mapping period in 2015; class-specific errors and burnt area were corrected according to Olofsson *et al* (2014). S-1A IW: Sentinel-1A Interferometric Wide swath.

S-1A IW acquisition date		Class: burnt	
Pre-fire	Post-fire	Omission error (%)	Commission error (%)
13 August	6 September	18	1
6 September	30 September	14	4
30 September	24 October	11	0
13 August	24 October	8	3

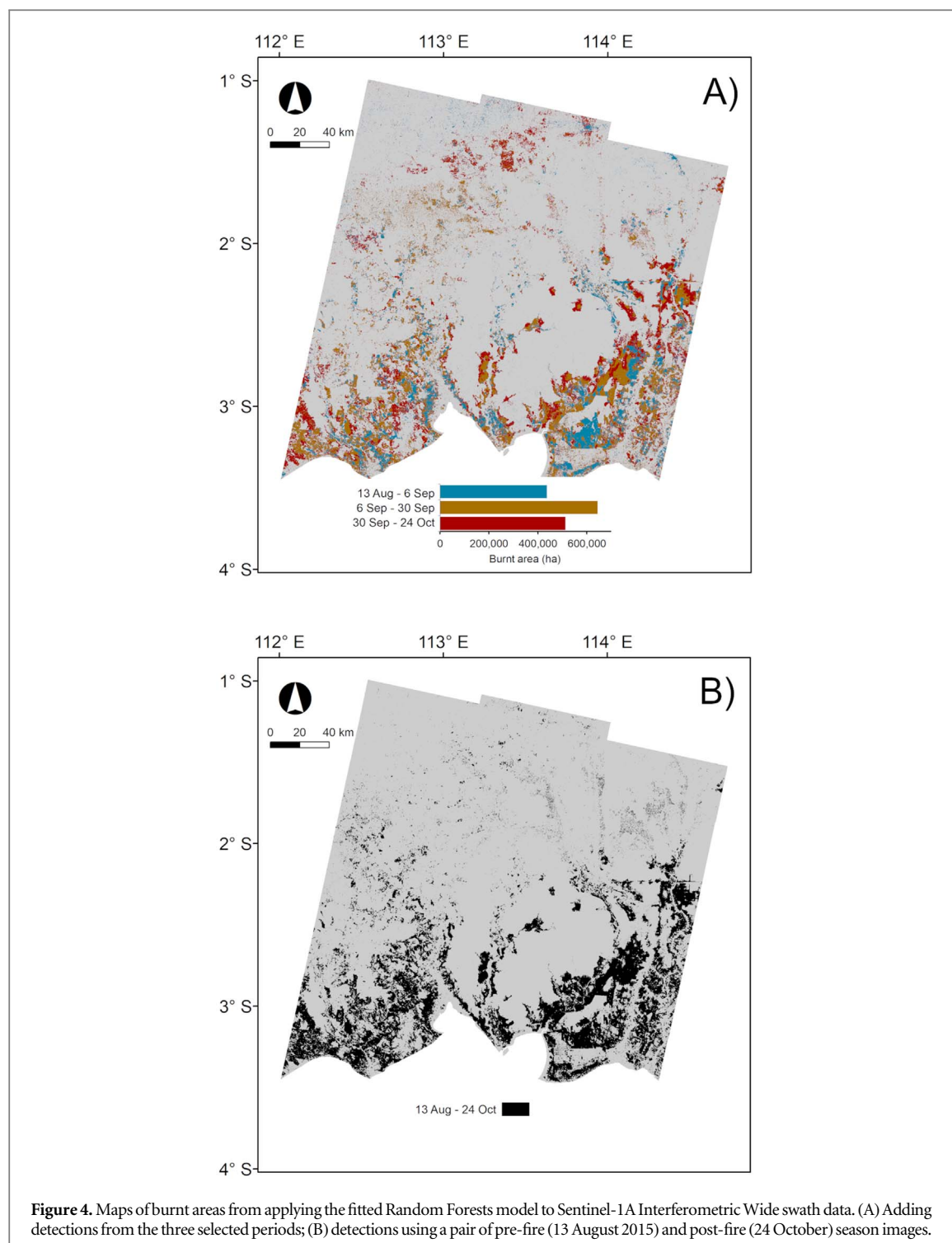
The fitted RF algorithm was applied to the three mapping periods during the fire season (table 1) and also to the pair of pre-fire and post-fire season images (13 August and 24 October). Table 2 depicts the omission and commission errors of the burnt class based on the test subset, corrected according to Olofsson *et al* (2014). The omission and commission errors of the unburnt class were always below 3% (not shown). The omission error of the burnt class ranged between 8% and 18%, with the commission error always below 5%.

Figure 4 displays the burnt area maps when (i) adding the detections from the three mapping periods and (ii) using a pair of pre-fire and post-fire season images. When combining the maps from the three distinct periods, some areas were mapped as burnt in more than one period, with these contributing approximately 29% to the overall burnt area. Of these, the vast majority (88%) were mapped as burnt in two

consecutive periods. When a pixel was mapped as burnt in more than one period, it was assigned as being burnt in the initial period, i.e. the burn detection in a subsequent period was assumed to result from a persistent fire scar. A total burnt area of 1593 413 ha was estimated when adding the detections from the three periods (figure 4(A)), whereas using a pair of pre-fire and post-fire season images resulted in a substantially smaller burnt area of 1164 435 ha. The two datasets (figures 4(A) and (B)) agree over 91% of the ~6 Mha study area (74% in unburnt areas and 17% in burnt areas). However, 2% of the area was mapped as unburnt when adding detections from the three periods (figure 4(A)) and as burnt when using pre-fire and post-fire season images (figure 4(B)). Conversely, 7% of the study area was mapped as burnt when adding detections from the three periods (figure 4(A)) and as unburnt when using pre-fire and post-fire season images (figure 4(B)). The area mapped as burnt in each period (figure 4(A)) and as unburnt in figure 4(B) represents between 26% (13 August–6 September) and 31% (20 September–24 October) of the total area mapped as burnt in each period. Hence, detecting fire scars from just pre-fire and post-fire season images significantly under-estimates burnt area, in this case giving 37% less than when adding detections from the three periods.

### 5.3. Comparison with existing maps of burnt area

Figure 5 shows the comparison at 5 km scale between the burnt area proportion obtained from this study



**Figure 4.** Maps of burnt areas from applying the fitted Random Forests model to Sentinel-1A Interferometric Wide swath data. (A) Adding detections from the three selected periods; (B) detections using a pair of pre-fire (13 August 2015) and post-fire (24 October) season images.

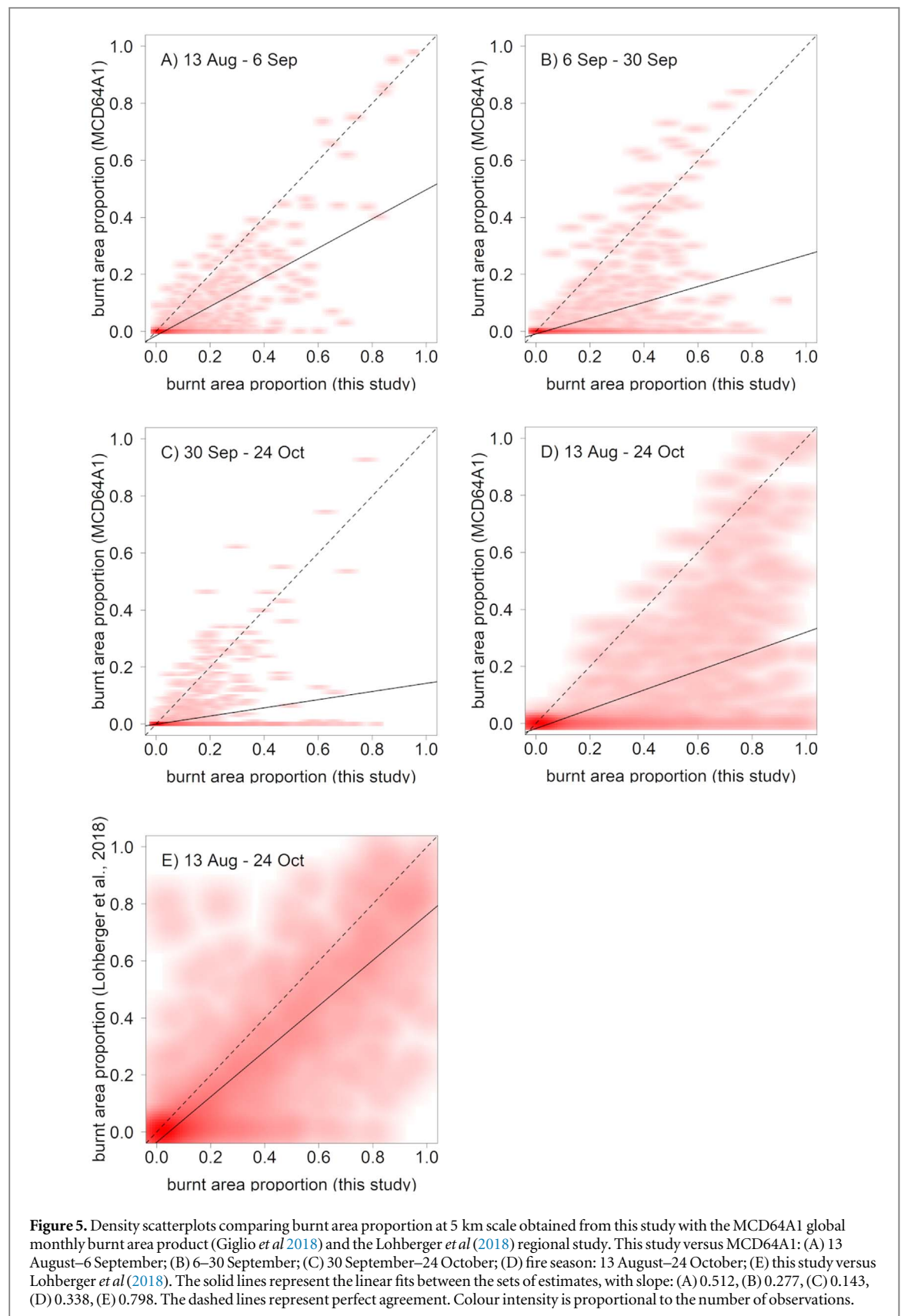
and those produced by the MCD64A1 global monthly burnt area product (Giglio *et al* 2018) and the Lohberger *et al* (2018) regional study.

The burnt area proportion obtained in this study is consistently much higher than from the MCD64A1 product. In the first period (13 August–6 September, figure 5(A)) the estimates of burnt area proportion from the MCD64A1 product are on average 51% of those obtained from this study. This value decreases to 28% and 14% in the second (6–30 September, figure 5(B)) and third (30 September–24 October, figure 5(C)) periods, respectively. During the fire

season (13 August–24 October, figure 5(D)) the estimates of burnt area proportion from the MCD64A1 product is on average 34% of those from this study.

Much better agreement is observed between our estimate of burnt area proportion during the fire season and that from Lohberger *et al* (2018) (figure 5(E)). The regression line has gradient 0.80 ( $R^2 = 0.82$ ) over the 5 km systematic grid. However, when compared with our overall estimate from adding the detections from the three periods (5 km grid = ~1.5 Mha), the overall burnt area from Lohberger *et al* (2018) is much smaller (5 km grid = ~1.0 Mha).





## 6. Discussion

The analysis in this paper makes clear that Sentinel-1 provides a powerful tool for mapping fire scars, and can yield important information about fire dynamics in the landscape. Also clear is that using

machine learning methods to extract this information is not straightforward since it involves decisions about the degree of confidence one has that a fire has occurred and the level of commission error (or false detections) that is acceptable, as we now discuss.

### 6.1. Algorithmic and data issues affecting discrimination of burnt areas with Sentinel-1 data

The empirical basis for detecting burnt area from S1-A data is clear from figure 2, which shows that both VH and VV intensity tend to decrease after a fire. At C-band, the VH backscatter from vegetated areas mainly arises from volume scattering from leaves and small branches, so tends to decrease when the canopy is lost due to fire. For VV the situation is more complicated, with backscatter mainly coming from canopy elements when the canopy is dense, but changing to surface and double bounce scattering after canopy loss by fire, especially when this allows penetration to the ground. Hence the observed reduction in VV backscatter cannot be predicted, and in some circumstances, fire scars may be brighter at VV than the surrounding intact forest, particularly if the soil is wet in these areas (Kasischke *et al* 1994).

We identified several factors that might explain the difference between the overall burnt area estimated from adding detections from three periods and when using a pair of pre-fire and post-fire season images (figures 4(A) and (B)):

- (a) The backscatter signal of a fire scar may fade quickly with time and therefore the scar may not be detected when only a pair of pre-fire and post-fire season images is used. We can point to anecdotal evidence of the fire scar signal fading with time, but do not have a precise estimate of how much of the difference might be due to this effect, which was mostly observed over areas mapped as burnt during the first period (13 August–6 September), therefore allowing the vegetation to recover before the end of the fire season.
- (b) The impact of soil moisture, mainly due to changing environmental conditions (rainfall events). This is more relevant to burnt area detection if the algorithm is choosing VV backscatter as a predictor.
- (c) The two maps have errors (see validation in table 2) and part of the mismatch will be due to the omission and commission errors in both approaches.

A known source of error in the methodology adopted here is that some changes in the landscape, especially clearcutting of forest, will produce backscatter changes similar to fire and will produce detections falsely ascribed to fire. The overall magnitude of the area affected by such non-fire changes that are mapped as burnt is unknown, but the extent of such false detections could be estimated if data about the location of forest concessions and their management plans were available. The World Resources Institute (WRI) Global Forest Watch (GFW) platform

(<https://globalforestwatch.org>) gives access to the location of forest concessions (including oil palm). For Indonesia, these data are provided by the Ministry of Forestry. It may also be possible to extract geometrical information from the detections in order to recognise the regular shapes expected under forest management, but this would require a substantial amount of development and testing.

Although errors due to clearcuts, for example, are inevitable under the methodology used, the primary control on the structure of the errors is the trade-off between omission and commission errors (figure 3) which involves decisions that are mostly qualitative and depend on the classification problem (Freeman and Moisen 2008). However, by adding information or refining the decision rules, it may be possible to reduce the commission errors, allowing higher detection rates to be achieved. For example, information on forest concessions could provide ancillary data that would allow a substantial proportion of commission errors to be eliminated. Furthermore, if we were to constrain the detected burnt areas to occur in patches greater than a minimum area, then a substantial component of these areas could be discarded by filtering processes.

Extending this approach to S-1 data at regional or global scales is highly desirable but would involve processing and storing data volumes many orders of magnitude greater than those from optical sensors currently used to estimate the global spatial distribution of burnt areas. It would also require generating a regional- or global-scale dataset of reference observations of unburnt and burnt locations, similar to the approach followed by Friedl *et al* (2010) when developing their algorithm to map land cover types globally at annual time steps using MODIS data (MCD12Q1).

### 6.2. Causes of mismatch with other maps of burnt area

Figures 3(A)–(D) shows that the estimates of burnt area by 5 km cell obtained from our study are almost always higher than those from MODIS (MCD64A1), and in all periods we observe many cells in which Sentinel sees a significant proportion as burnt while the MODIS data shows almost no burn. The MODIS product is based on optical sensors, so is hindered by smoke and cloud cover, which in this region and season is likely to be very high (table S2, supplementary information). Daily fractional cloud cover derived from the Terra sensor (the MOD06\_L2 product) (Platnick *et al* 2015) was available at a spatial resolution of ~5 km and covered the 13 August–24 October 2015 period analysed in this study. This was averaged by mapping period over areas detected as burnt in this study. A considerable disagreement between the burnt area estimates from this study and MODIS occurred during those periods of higher fractional cloud cover, which had values 46%, 61% and 67% in the periods

13 August–6 September, 6 September–30 September and 30 September–24 October, respectively. The clear implication is that the MODIS estimates are severely affected by cloud cover (as one would expect), resulting in underestimation of burnt areas and hence GHG emissions in this region.

The estimates of burnt area from Lohberger *et al* (2018) were obtained using a set of S-1A IW scenes acquired before and after the 2015 fire season (20 June and 24 October respectively) covering Kalimantan, Sumatra and West Papua. However, we show that this is likely to have missed a significant proportion of burnt area. There is much better agreement with the estimates from Lohberger *et al* (2018) (figure 5(E)) than with those from MODIS data (figures 5(A)–(D)) but our study clearly demonstrates that not using multiple S-1A IW acquisitions during the fire season resulted in a decreased detection of burnt areas of approximately 33%: 1.5 Mha in our study against 1.0 Mha in Lohberger *et al* (2018).

The constellation of S-1A and S-1B IW acquisitions will provide an unprecedented, unique capability to observe all landmasses every 12 d at ~10 m spatial resolution without having to consider issues related to cloud cover. Giglio *et al* (2013) observe that persistent cloud cover is a severe obstacle to detecting active fires and fire scars and that this could lead to systematic underestimation of burnt area in areas with continual cloud cover. This was also recognised by van der Werf *et al* (2010) as one of the most significant uncertainties when estimating global fire emissions from burnt area products in tropical regions. Huijnen *et al* (2016) estimated the carbon emissions from the Indonesian fires in 2015 using estimates of the fire radiative power (FRP) provided by the MODIS sensors onboard Terra and Aqua. They note that this system could underestimate active fire detections (and hence the corresponding FRP estimates) because of persistent cloud cover and smoke over currently burning areas.

## Acknowledgments

The re-projected monthly GeoTIFF version of the MODIS MCD64A1 burnt area product was made available by the University of Maryland. The daily MODIS MCD14ML active fire product was produced by the University of Maryland and provided by NASA FIRMS operated by NASA/GSFC/ESDIS with funding provided by NASA/HQ. The daily Terra MODIS MOD06\_L2 fractional cloud cover product was downloaded from NASA's Level-1 and Atmosphere Archive & Distribution System (LAADS) Distributed Active Archive Center (DAAC). We acknowledge and thank ESA CCI Fire for providing access to a burnt area map of Kalimantan. JMBC and SQ were supported by the Natural Environment Research Council (Agreement PR140015 between NERC and the National Centre for Earth Observation).

## Data availability statement

The data that support the findings of this study are available upon request from the authors.

## ORCID iDs

Joao M B Carreiras  <https://orcid.org/0000-0003-2737-9420>

Shaun Quegan  <https://orcid.org/0000-0003-4452-4829>

Kevin Tansey  <https://orcid.org/0000-0002-9116-8081>

Susan Page  <https://orcid.org/0000-0002-3392-9241>

## References

- Breiman L 2001 Random forests *Mach. Learn.* **45** 5–32
- Butler D 2014 Earth observation enters next phase *Nature* **508** 160–1
- Chuvieco E, Yue C, Heil A, Mouillot F, Alonso-Canas I, Padilla M, Pereira J M, Oom D and Tansey K 2016 A new global burned area product for climate assessment of fire impacts *Glob. Ecol. Biogeogr.* **25** 619–29
- De Zan F and Guarnieri A M 2006 TOPSAR: terrain observation by progressive scans *IEEE Trans. Geosci. Remote Sens.* **44** 2352–60
- Fortier J, Rogan J, Woodcock C E and Runfola D M 2011 Utilizing temporally invariant calibration sites to classify multiple dates and types of satellite imagery *Photogramm. Eng. Remote Sens.* **77** 181–9
- Freeman E A and Moisen G G 2008 A comparison of the performance of threshold criteria for binary classification in terms of predicted prevalence and kappa *Ecol. Modell.* **217** 48–58
- Friedl M A, Sulla-Menashe D, Tan B, Schneider A, Ramankutty N, Sibley A and Huang X M 2010 MODIS collection 5 global land cover: algorithm refinements and characterization of new datasets *Remote Sens. Environ.* **114** 168–82
- Giglio L, Boschetti L, Roy D P, Humber M L and Justice C O 2018 The collection 6 MODIS burned area mapping algorithm and product *Remote Sens. Environ.* **217** 72–85
- Giglio L, Justice C, Boschetti L and Roy D 2015 MCD64A1 MODIS/Terra + Aqua Burned Area Monthly L3 Global 500 m SIN Grid V006 [Data set]. NASA EOSDIS Land Processes DAAC/MCD64A1 MODIS/Terra+Aqua Burned Area Monthly L3 Global 500m SIN Grid V006 [Data set]. NASA EOSDIS Land Processes DAAC (Sioux Falls, SD, USA) (<https://doi.org/10.5067/MODIS/MCD64A1.006>)
- Giglio L, Loboda T, Roy D P, Quayle B and Justice C O 2009 An active-fire based burned area mapping algorithm for the MODIS sensor *Remote Sens. Environ.* **113** 408–20
- Giglio L, Randerson J T and van der Werf G R 2013 Analysis of daily, monthly, and annual burned area using the fourth-generation global fire emissions database (GFED4) *J. Geophys. Res.-Biogeosci.* **118** 317–28
- Gregoire J M, Tansey K and Silva J M N 2003 The GBA2000 initiative: developing a global burnt area database from SPOT-VEGETATION imagery *Int. J. Remote Sens.* **24** 1369–76
- Hansen M C *et al* 2013 High-resolution global maps of 21st-century forest cover change *Science* **342** 850–3
- Harris N L, Brown S, Hagen S C, Saatchi S S, Petrova S, Salas W, Hansen M C, Potapov P V and Lutsch A 2012 Baseline map of carbon emissions from deforestation in tropical regions *Science* **336** 1573–6
- Huijnen V, Wooster M J, Kaiser J W, Gaveau D L A, Flemming J, Parrington M, Inness A, Murdiyarso D, Main B and

- Van Weele M 2016 Fire carbon emissions over maritime southeast Asia in 2015 largest since 1997 *Sci. Rep.* **6** 26886
- Kasischke E S, Bourgeauchavez L L and French N H F 1994 Observations of variations in ERS-1 SAR image intensity associated with forest-fires in Alaska *IEEE Trans. Geosci. Remote Sens.* **32** 206–10
- Lambin E F, Geist H J and Lepers E 2003 Dynamics of land-use and land-cover change in tropical regions *Annu. Rev. Environ. Resour.* **28** 205–41
- Lohberger S, Stängel M, Atwood E C and Siegert F 2018 Spatial evaluation of Indonesia's 2015 fire-affected area and estimated carbon emissions using Sentinel-1 *Glob. Change Biol.* **24** 644–54
- Menges C H, Bartolo R E, Bell D and Hill G J E 2004 The effect of savanna fires on SAR backscatter in northern Australia *Int. J. Remote Sens.* **25** 4857–71
- Miettinen J, Langner A and Siegert F 2007 Burnt area estimation for the year 2005 in Borneo using multi-resolution satellite imagery *Int. J. Wildland Fire* **16** 45–53
- Miettinen J, Shi C and Liew S C 2016 Land cover distribution in the peatlands of Peninsular Malaysia, Sumatra and Borneo in 2015 with changes since 1990 *Glob. Ecol. Conservation* **6** 67–78
- Moreira A, Prats-Iraola P, Younis M, Krieger G, Hajnsek I and Papathanassiou K P 2013 A tutorial on synthetic aperture radar *IEEE Geosci. Remote Sens. Mag.* **1** 6–43
- Olofsson P, Foody G M, Herold M, Stehman S V, Woodcock C E and Wulder M A 2014 Good practices for estimating area and assessing accuracy of land change *Remote Sens. Environ.* **148** 42–57
- Page S E, Siegert F, Rieley J O, Boehm H D V, Jaya A and Limin S 2002 The amount of carbon released from peat and forest fires in Indonesia during 1997 *Nature* **420** 61–5
- Platnick S, Ackerman S A, King M D, Meyer K, Menzel W P, Holz R E, Baum B A and Yang P 2015 *MODIS Atmosphere L2 Cloud Product (06\_L2)*, NASA MODIS Adaptive Processing System (Greenbelt, MD: Goddard Space Flight Center) ([https://doi.org/10.5067/MODIS/MOD06\\_L2.006](https://doi.org/10.5067/MODIS/MOD06_L2.006))
- Quegan S and Yu J J 2001 Filtering of multichannel SAR images *IEEE Trans. Geosci. Remote Sens.* **39** 2373–9
- Randerson J T, Chen Y, van der Werf G R, Rogers B M and Morton D C 2012 Global burned area and biomass burning emissions from small fires *J. Geophys. Res.-Biogeosci.* **117** G04012
- Reiche J *et al* 2016 Combining satellite data for better tropical forest monitoring *Nat. Clim. Change* **6** 120–2
- Richards J A 2009 *Remote Sensing with Imaging Radar* (Heidelberg, New York: Springer)
- Schroeder W, Csizsar I and Morissette J 2008 Quantifying the impact of cloud obscuration on remote sensing of active fires in the Brazilian Amazon *Remote Sens. Environ.* **112** 456–70
- Sedano F, Kempeneers P, Miguel J S, Strobl P and Vogt P 2013 Towards a pan-European burnt scar mapping methodology based on single date medium resolution optical remote sensing data *Int. J. Appl. Earth Obs. Geoinf.* **20** 52–9
- Siegert F and Hoffmann A A 2000 The 1998 forest fires in East Kalimantan (Indonesia): a quantitative evaluation using high resolution, multitemporal ERS-2 SAR images and NOAA-AVHRR hotspot data *Remote Sens. Environ.* **72** 64–77
- Silva J M N, Sa A C L and Pereira J M C 2005 Comparison of burned area estimates derived from SPOT-VEGETATION and Landsat ETM plus data in Africa: influence of spatial pattern and vegetation type *Remote Sens. Environ.* **96** 188–201
- Simon M, Plummer S, Fierens F, Hoelzemann J J and Arino O 2004 Burnt area detection at global scale using ATSR-2: the GLOBSCAR products and their qualification *J. Geophys. Res.-Atmos.* **109** D14S02
- Torres R *et al* 2012 GMES Sentinel-1 mission *Remote Sens. Environ.* **120** 9–24
- Tyukavina A, Baccini A, Hansen M C, Potapov P V, Stehman S V, Houghton R A, Krylov A M, Turubanova S and Goetz S J 2015 Aboveground carbon loss in natural and managed tropical forests from 2000 to 2012 *Environ. Res. Lett.* **10** 074002
- van der Werf G R, Randerson J T, Giglio L, Collatz G J, Mu M, Kasibhatla P S, Morton D C, Defries R S, Jin Y and Van Leeuwen T T 2010 Global fire emissions and the contribution of deforestation, savanna, forest, agricultural, and peat fires (1997–2009) *Atmos. Chem. Phys.* **10** 11707–35
- Woodhouse I H 2006 *Introduction to Microwave Remote Sensing* (Boca Raton, FL: Taylor and Francis)
- Wooster M J, Xu W and Nightingale T 2012 Sentinel-3 SLSTR active fire detection and FRP product: pre-launch algorithm development and performance evaluation using MODIS and ASTER datasets *Remote Sens. Environ.* **120** 236–54